

# 3D-Printed Polyetheretherketone Smart Polymer Nanocomposite Scaffolds: Mechanical, Self-Sensing, and Biological Attributes

Johannes Schneider, Srijani Basak, Yanan Hou, Joseph H. Koo, Brian L. Wardle, Nikolaj Gadegaard, and Shanmugam Kumar\*

This study demonstrates the mechanical, self-sensing, and biological characteristics of carbon nanotubes (CNTs) and graphene nanoplatelets (GNPs)-engineered 3D-printed polyetheretherketone (PEEK) composite scaffolds, utilizing custom-made feedstocks. Microstructural analysis and macroscale testing reveal that the PEEK/CNT scaffolds with 6 wt% CNT content and 46% relative density achieve a gauge factor of up to 75, a modulus of 0.64 GPa, and a compressive strength of 64 MPa. The PEEK/CNT2.5/GNP2.5 scaffolds evince still better performance, at a relative density of 73%, reporting a modulus of up to 1.1 GPa and a compressive strength of 122 MPa. Importantly, stability in mechanical and piezoresistive performance up to 500 cycles is noted, indicating a durable and reliable performance under cyclic loading. Murine preosteoblast cells (MC3T3-E1) are used to biologically characterize sulfonated scaffolds over 14 days. Cytotoxicity, DNA, and alkaline phosphatase (ALP) levels are quantified through in vitro assays, evaluating cell viability, proliferation, and osteogenic properties. Notably, PEEK/CNT 6 wt% scaffolds exhibit nearly 80% cytocompatibility, while PEEK/CNT2.5/GNP2.5 scaffolds reach nearly 100%. Both types of scaffolds support cell differentiation, as evidenced by elevated ALP levels. These findings carry significant promise in bone tissue engineering, paving the way for the development of adaptive, intelligent structural implants boasting enhanced biocompatibility and self-sensing capabilities.


bone physiology, presenting PEEK as a promising biomaterial for creating engineered bone tissue. Enhancements to implants are being addressed by developing self-sensing smart materials, offering real-time in vivo feedback. PEEK is a thermoplastic polymer with a semicrystalline structure. It has emerged as a promising implant material for bone repair and regeneration purposes, due to its excellent mechanical properties, resistance to chemicals and heat, and excellent biocompatibility.<sup>[1]</sup> PEEK demonstrates minimal local or systemic toxicity, making it suitable for a wide range of applications in industries such as automotive, aerospace, electrical, chemical, military, and healthcare.<sup>[2–5]</sup> With a modulus of 3–4 GPa, PEEK can be tailored to achieve Young's modulus comparable to cortical bone.<sup>[6]</sup> Furthermore, PEEK's radiolucency is advantageous in biomedical applications, as it allows for clear and accurate imaging of surrounding anatomical structures during medical procedures without any interference from the material itself.<sup>[7]</sup> This presents a significant advantage over titanium, the current industry

gold standard for implant materials. Among the array of biomaterials, steel stands out for its robust strength and ductility; however, it succumbs easily to corrosion and lacks adequate wear resistance.<sup>[8]</sup> In stark contrast, CoCrMo alloys exhibit remarkable wear resistance and strength, yet pose the risk of triggering allergic reactions due to the presence of nickel, chromium, and

## 1. Introduction

Advances in high-temperature polymer additive manufacturing (AM) using polyetheretherketone (PEEK) structural polymers have enabled new capabilities in composites and particularly the creation of patient-specific orthopedic implants mimicking

J. Schneider, S. Basak, N. Gadegaard, S. Kumar  
James Watt School of Engineering  
University of Glasgow  
Glasgow G12 8QQ, UK  
E-mail: msv.kumar@glasgow.ac.uk

 The ORCID identification number(s) for the author(s) of this article can be found under <https://doi.org/10.1002/adem.202301659>.

© 2024 The Authors. Advanced Engineering Materials published by Wiley-VCH GmbH. This is an open access article under the terms of the Creative Commons Attribution License, which permits use, distribution and reproduction in any medium, provided the original work is properly cited.

DOI: 10.1002/adem.202301659

Y. Hou, J. H. Koo  
Walker Department of Mechanical Engineering  
The University of Texas at Austin  
204 E Dean Keeton St, Austin TX 78712, USA

B. L. Wardle  
J Department of Aeronautics and Astronautics  
Massachusetts Institute of Technology  
77 Massachusetts Ave, Cambridge, Massachusetts 02139, USA

B. L. Wardle  
Department of Mechanical Engineering  
Massachusetts Institute of Technology  
77 Massachusetts Ave, Cambridge, Massachusetts 02139, USA

cobalt.<sup>[9]</sup> Ceramics, although known for their hardness and compatibility with biological tissues, suffer from brittleness and inflexibility.<sup>[10]</sup> On the other hand, polymers, characterized by their lightweight and flexibility, face challenges in sterilization and wear resistance and are prone to absorbing water and proteins at an accelerated rate.<sup>[11]</sup> A comprehensive review of biomaterials for orthopedic surgery, including detailed physical characteristics of bone, is provided by Szczęśny et al.<sup>[12]</sup>

Medical-grade PEEK is poorly soluble in water, which prevents it from degrading in a fluid environment and allows it to retain its mechanical properties during long-term fluid exposure. However, the low solubility of PEEK, along with its resonance-stabilized aromatic backbone, makes it extremely bioinert, reducing its affinity for cell attachment in vivo and preventing implant anchorage to adjacent bone tissue.<sup>[13]</sup> This can elicit inflammatory reactions from the surrounding biological environment, or cause the formation of fibrous encapsulations around the implant, leading to instability and undesirable migration of the implant to other parts of the body. Cell affinity and attachment on PEEK surfaces can be enhanced through various methods and remain a field of active research. Common methods include surface modification techniques, such as sulfonation,<sup>[14,15]</sup> micropatterning, or coating with bone-binding mineral powders, such as hydroxyapatite (HA) or functionalization with bioactive molecules.<sup>[16,17]</sup> Recent studies suggest that the integration of bioactive fillers such as HA or bioactive glass could enhance the osteoconductivity of PEEK composites. These fillers have been shown to improve cellular response and bone bonding, addressing the challenge of PEEK's bioinertness.<sup>[18]</sup> Furthermore, advanced 3D printing techniques have been utilized to create PEEK/HA composites with up to 30 wt% HA, highlighting the adaptability of PEEK matrices to high filler loadings and their potential in patient-specific devices and implants.<sup>[19]</sup>

Segmental bone defects resulting from high-impact trauma, and osteodegenerative diseases, present significant clinical challenges. Reconstructive surgery is often tedious and risky due to its postoperative impact on bone function and aesthetics.<sup>[20]</sup> It can lead to prolonged recovery periods, diminished quality of life post-surgery, and impose a substantial economic burden on the healthcare system. Bone loss resulting from critical fractures, tumor resection, or osteoporosis often requires the use of multiple therapeutic methods such as corrective surgery, radiation, and targeted drug administration.<sup>[21]</sup> Supplements of exogenous scaffolds are used to support reconstruction and facilitate the regeneration of surrounding soft tissue.<sup>[22]</sup> Despite autografts

or allografts being conventionally used, this procedure has limitations such as immunogenic reactions, postoperative pain, graft and donor site morbidity, and structural imperfections. Hence, the advent of synthetic bone implants and prostheses becomes imperative.<sup>[23]</sup> Initially, the development of engineered bone tissues and scaffolds started out with meeting the mechanical requirements and stabilization of the host tissue. Considerations were eventually required for favorable biological interaction between the host tissue and the implant, to ensure that the implant, besides maintaining mechanical stability, did not induce an immunogenic reaction or microbial infections.<sup>[24]</sup>

In recent years, significant advancements have been achieved through AM of high-temperature polymers such as PEEK.<sup>[25]</sup> The cost-effective AM technique for processing PEEK is fused filament fabrication (FFF), where heated filament feedstock is extruded through a nozzle onto a build plate, enabling layer-by-layer fabrication of objects.<sup>[26–29]</sup> Additionally, selective laser sintering (SLS), an alternative, but slightly expensive 3D printing technique increasingly being explored with PEEK, involves selectively fusing powdered feedstock using a laser, scanning, and melting thin cross sections of the powder to progressively form precise and solid objects. These advancements have revolutionized the fabrication of complex cellular implants, making them increasingly viable in the biomedical domain,<sup>[30–33]</sup> enabling the creation of patient-specific implants that mimic the inhomogeneous stiffness of native bone, thereby minimizing stress shielding.

Stress shielding (**Figure 1**) occurs when the implant material absorbs a significant portion of the mechanical load, resulting in reduced stress transfer to the surrounding bone, caused by a stiffness mismatch with the native bone.<sup>[34]</sup> This phenomenon can lead to bone resorption, weakened bone structure, and potential loosening or failure of the implant. In comparison to titanium, PEEK composites offer a more flexible and less rigid composition, capable of closely matching Young's modulus of natural bone. This characteristic helps alleviate stress shielding effects by facilitating efficient load transfer between the implant and the surrounding bone. Consequently, PEEK implants promote a more uniform stress distribution, reducing the risk of bone loss and enhancing long-term implant stability compared to titanium implants. To further enhance the resemblance with bone properties, the stiffness match can be improved by gradually grading the relative density of cellular PEEK. This allows for fine-tuning of the implant's stiffness. Moreover, cellular implants offer a high surface area density ( $\text{mm}^2/\text{mm}^3$ ), which promotes favorable bone cell proliferation, attachment, and accelerated osseointegration.<sup>[35]</sup>

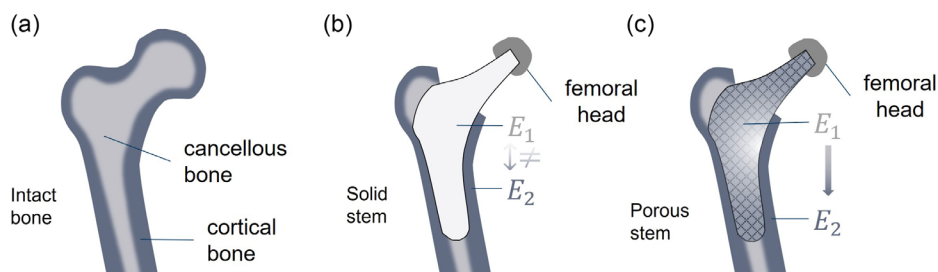


**Figure 1.** Schematic representation of stress shielding: a) uncompromised bone illustrating seamless gradation between cortical and cancellous bone regions, b) solid stem implant inserted into compromised bone, exhibiting stiffness mismatch ( $E_1$  and  $E_2$ ) between the implant and native bone material, and c) porous stem implant facilitating a spatially tailored transition of mechanical properties, between implant and surrounding bone tissue.

Note that the relative density is the solid volume fraction of the cellular material/scaffold, denoted by  $\bar{\rho}$ .

While PEEK (neat) is nearly electrically nonconductive, electrically conductive micro- and/or nanofillers can be incorporated to enhance its electrical conductivity by several orders of magnitude and use the resulting PEEK composite as a smart material. Electrical conductivity can be imparted through several conduction mechanisms, such as interaggregate conduction and tunneling of electrons (not applicable to microscale fillers).<sup>[36,37]</sup> If enough electrically conductive fillers are added to the PEEK matrix, they will establish electrical percolation and the resulting PEEK composite will be electrically conductive. The effectiveness of the conductive network in the composite depends on the separation or contact between fillers, where filler contact or electron jumping through a thin polymer layer facilitates conduction within the matrix. To avoid agglomeration and achieve optimum performance, it is essential to achieve a high-quality filler dispersion in the polymer matrix. Agglomeration can lead to an uneven distribution of electrical and mechanical properties and, interestingly, it can even lead to higher electrical conductivity at lower filler loadings due to the formation of segregated filler structures.<sup>[36]</sup> The quality of the conductive network is closely related to the formation of a percolation network. Although higher filler loadings typically correlate with higher conductivity, segregated structures can form at lower loadings and contribute to the development of a conductive network. Common fillers used to achieve this conductive network include carbon fibers (CF), carbon nanotubes (CNTs), or graphene nanoplatelets (GNP).

Mohiuddin and Hoa<sup>[38]</sup> conducted a study on the electrical conductivity of a nanomodified PEEK/CNT composite. They examined the piezoresistive behavior at various temperatures and filler contents and identified a percolation threshold of  $\approx 3.5$  wt%. In their study, Arif et al.<sup>[26]</sup> investigated the thermo-physical, mechanical, and wear properties of GNP- and CNT-reinforced electrically conductive PEEK nanocomposites processed via the FFF technique. Their findings revealed that both GNP and CNT reinforcements led to a reduction in the coefficient of thermal expansion compared to neat PEEK. This reduction in thermal expansion coefficient contributes to improved dimensional stability of the resulting structures. In their research, Gonçalves et al.<sup>[39]</sup> developed electrically conductive PEEK nanocomposite filaments specifically designed for FFF, successfully incorporating CNTs and GNPs. The inclusion of CNTs resulted in an electrical conductivity of  $10 \text{ S m}^{-1}$ , accompanied by enhanced mechanical properties and thermal conductivity. On the other hand, the addition of GNPs improved the melt processability of the filaments, maintained the electrical conductivity at the desired levels, and reduced the coefficient of friction by up to 60%. In their work, Alam et al.<sup>[35]</sup> demonstrated the incorporation of CNTs and GNPs into the PEEK matrix, along with sulfonation of their 3D-printed cellular specimens. Their findings revealed that this combination promotes bioactivity, leading to substantial mineralization. Additionally, reinforced sulfonated PEEK exhibited improved mechanical performance, presenting design opportunities for personalized bioactivated surfaces and the potential for smart and multifunctional structures.<sup>[35,40,41]</sup>

This work seeks to fill the gap in the research regarding nanomodified, multifunctional PEEK cellular scaffolds intended for biomedical applications. PEEK and its nanocomposites have

been investigated for their potential utilization as engineered orthopedic scaffolds in the medical industry. The integration and monitoring of implants within the human body pose recurrent challenges and often require time-intensive, meticulous, and routine monitoring, to ensure proper retention and functioning of the device. To overcome this, self-sensing smart materials are developed that can provide real-time feedback on the condition and position of the implant in vivo. This study focuses on the mechanical, piezoresistive, self-sensing, and biological characteristics of smart PEEK cellular nanocomposites processed via FFF technique using in-house nanoengineered filament feedstocks comprising multi-walled CNTs (MWCNTs) and/or GNPs. Custom-made PEEK (neat) and PEEK composites with 6 wt% MWCNTs, 5 wt% GNPs, and a combination of CNTs and GNPs with 2.5 wt% each were explored. Filaments with a diameter of 1.75 mm were produced via a melt blending technique using a corotating twin-screw extruder. In alignment with our focus on the self-sensing properties of PEEK, the initial decision to forgo bioactive fillers allowed a concentrated exploration of the fundamental mechanical and piezoresistive characteristics of nanocarbon-incorporated PEEK scaffolds. The scaffolds were designed with different porosities while maintaining constant feature sizes of  $480 \mu\text{m}$ . The scaffolds were tested under monotonic compression up to densification and quasistatic cyclic compression with a 3% strain amplitude. The mechanical and piezoresistive performance, indicated by the normalized change in electrical resistance ( $-\Delta R/R_0$ ), is reported as a function of strain and the number of cycles. In vitro assays for cytotoxicity, DNA quantification, and alkaline phosphatase (ALP) activity were performed on MC3T3-E1 cells cultured on the scaffolds, to assess the influence of the scaffold material and relative density on cell viability, proliferation, and differentiation. The tunable self-sensing and enhanced mechanical performances of PEEK nanocomposite lattices were experimentally demonstrated with a particular focus on strain and damage sensing. Different piezoresistive trends were observed for CNT- and GNP-modified composites. Results obtained from biological analysis, as fluorescence and absorbance data, were used to determine percentage viability of cells, with the concentrations of DNA and ALP expressed. The study's collective findings offer valuable insights into the design and development of smart piezoresistive PEEK composites for structural, functional, and biomedical applications, enabling in vivo and in situ structural health monitoring.

## 2. Experimental Section

### 2.1. Geometric Modeling

Cubic scaffolds with a dimension of  $10 \times 10 \times 10 \text{ mm}^3$  as well as cylindrical scaffolds with a diameter of 10 mm and height of 2 mm were created using SolidWorks (Dassault Systèmes SolidWorks Corporation). The scaffolds were characterized by a rectangular, porous pattern, designed such, that they could be manufactured in a single nozzle movement, without it having to interrupt its designated path to complete the final structure, independent of the number of layers chosen. This allows for a higher resolution compared to structures with ordinary random print paths, as the walls were built based on a single continuous extrusion. Though various designs for architected cellular solids

were conceived and explored to enhance stiffness, strength, or energy absorption,<sup>[29,42]</sup> the complexity of these cellular architectures often demanded thorough process optimization for successful fabrication through FFF, particularly when utilizing PEEK with reinforcing fibers. As a result, this study intentionally focused on developing a design with a straightforward cellular geometry, meticulously optimized for effortless manufacturing on a smaller scale achievable through FFF 3D printing. The wall thickness of the scaffolds here, the same as the extrusion width, was set consistently to 480  $\mu\text{m}$ , while pore sizes of 720, 470, and, 200  $\mu\text{m}$  were considered. The corresponding relative density  $\bar{\rho} = \rho_c/\rho$ , the ratio between the density of the cellular structure  $\rho_c$  to the density of the parent material  $\rho$ , was 46%, 55%, and 73%, respectively. The selection of pore sizes (and porosity level) was dictated by the design space and extrusion width. Within this design space, accommodating 2–20 bead paths was feasible. Opting for 9, 11, and 15 extrusion counts, we sought a balance to circumvent overly large gaps or high material density. This method potentially allowed for spatially grading density to reduce stress shielding, as discussed in the introduction section. The height of each layer was set to 100  $\mu\text{m}$ . **Figure 2** displays a schematic that encompasses filament synthesis, 3D geometric modeling, FFF and, mechanical, piezoresistive, and biological characterizations.

## 2.2. Materials

The materials used in this study to fabricate lattice structures were custom-made PEEK (neat), and PEEK nanocomposites with 6 wt% MWCNT, namely PEEK/CNT6. Further, a nanocomposite

with 5 wt% GNP, and a combination of CNT and GNP with 2.5 wt% each, were also explored, namely, PEEK/GNP5 and PEEK/CNT2.5/GNP2.5, respectively. Filaments with a diameter of 1.75 mm were produced via melt blending technique using a corotating twin-screw extruder. The PEEK utilized was KetaSpire PEEK (KT-880 NT) supplied by Solvay, and the MWCNT was Graphistrength C100 MWCNT provided by Arkema. The nanoparticles were incorporated into PEEK pellets in increments not exceeding 1 wt% each time. For instance, the PEEK/CNT2.5/GNP2.5 composite commenced with the addition of 1 wt% CNT to the PEEK pellets. The CNT powder and PEEK pellets were initially mixed using a Thinky mixer before being introduced into a twin-screw extruder for melt blending (see, Figure S1, Supporting Information). The temperatures set in the various sections of the twin-screw extruder ranged from 340 to 370  $^{\circ}\text{C}$ , in the following sequence from left to right: 340, 350, 363, 363, 363, 363, 360, and 370  $^{\circ}\text{C}$ .

Filaments of PEEK containing 1 wt% CNT were extruded ( $\approx 2$  kg in total) and air cooled before being wound onto a spool using the Filabot filament winder. Subsequently, the filaments were cut into pellets (particles) by a pelletizer, as illustrated in Figure S2 (Supporting Information). These pellets underwent an additional filament extrusion process to improve blending. The pelletizing and extrusion procedures were iteratively performed until smooth and uniformly textured filaments were obtained. Additional CNT and GNP powders were then incorporated. For the final extrusion, a caliper was employed to sample the diameter of the filaments before spooling, aiming to maintain dimensions within the range of  $1.75 \pm 0.15$  mm.

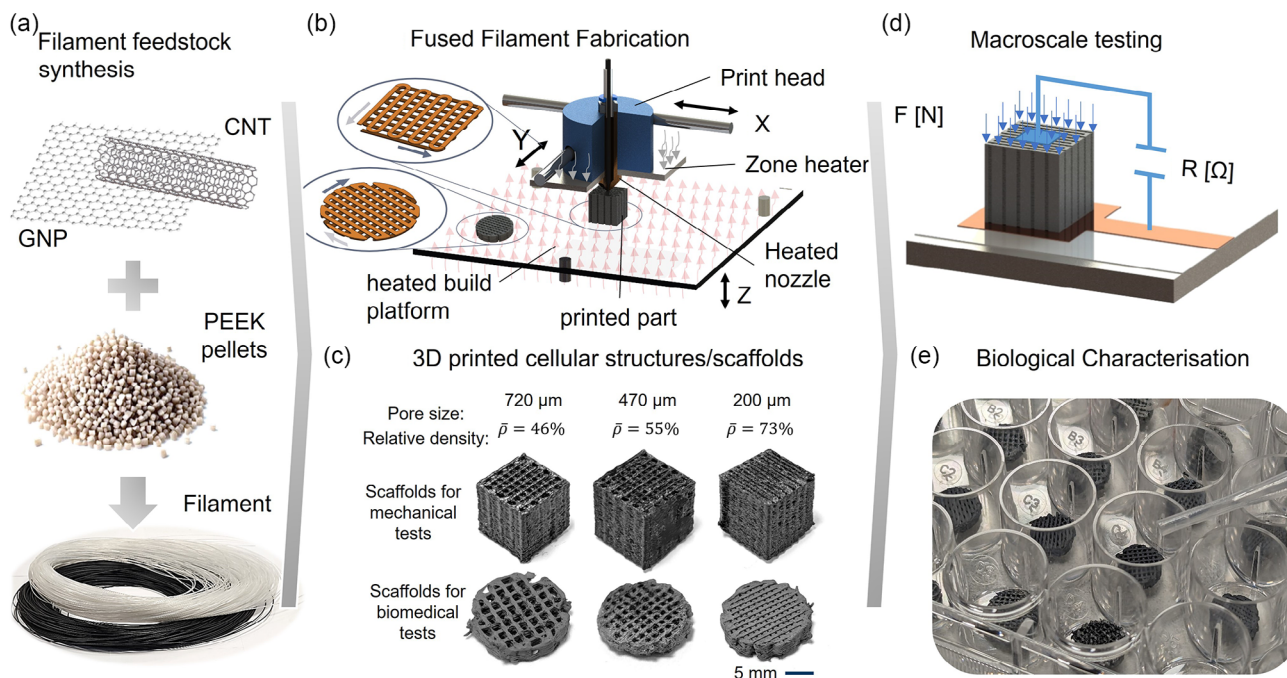


**Figure 2.** a) Diagram illustrating the filament fabrication process incorporating CNT and GNP nanofillers. b) Schematic representation of the FFF process, showcasing c) sample scaffolds produced using PEEK/CNT6 (6 wt% MWCNT) for subsequent d) mechanical and e) biomedical analyses. The diagram elucidates the 3D printing principle for achieving high-resolution continuous printing paths, facilitating the creation of cubic or cylindrical scaffolds with controlled porosities. Right: Schematic depiction of the compression test setup, encompassing piezoresistive measurements and the biological characterization of samples placed within well plates.

### 2.3. FFF of Bulk and Scaffold Samples

Bulk and cellular specimens were printed using FFF with an Apium P220 3D printer. In FFF, thermoplastic filament, with a diameter of 1.75 mm, was fed from a spool to the print head, where it was heated and extruded through a nozzle with a diameter of 0.4 mm onto a build plate. The build plate can move vertically, while the print head moved horizontally, following the print path specified by the computer-generated code (G-code), depositing the material layer by layer. The G-code was created using Simplify3D software. Consistent printing parameters were used for all composites, including a layer height of 100  $\mu\text{m}$ , an extruder temperature of 450–470  $^{\circ}\text{C}$ , a bed temperature of 120–150  $^{\circ}\text{C}$ , and a printing speed for the scaffold of 480–800  $\text{mm min}^{-1}$ . For PEEK/CNT6 alone, the printing speed was lowered, as it proved to be an effective strategy for this composite to overcome the challenges posed by the fluctuating diameter of the filament feedstock, thereby attaining superior printing outcomes. The default printing parameters for each material are listed in Table S2 (Supporting Information). The printer incorporated a zone heater positioned above the nozzle. The heater offered targeted heating onto the structure as it was built, during the printing process, maintaining a temperature slightly below the polymer's glass transition temperature. This approach enhanced the crystallinity of the PEEK 3D-printed part while concurrently achieving superior surface quality and improved layer adhesion.<sup>[43]</sup> As a result, the lower sections of the component remained more rigid, allowing for enhanced resolution compared to fully heated build chambers. To remove any remaining moisture from the filament feedstock, it was dried at 60  $^{\circ}\text{C}$  for at least 24 h before printing.

### 2.4. Mechanical Testing

#### 2.4.1. Tensile and Compression Tests

Tensile tests were conducted on bulk specimen following ASTM D638 with type V specimens, while compression tests were performed according to ASTM D695 using cuboids of  $12.7 \times 12.7 \times 25.4 \text{ mm}^3$ . Both tests were performed on a Zwick 250 universal testing machine (UTM) equipped with a 250 kN load cell at a test speed of 2  $\text{mm min}^{-1}$ . Similarly, cellular samples were tested under compression with a loading rate of 2  $\text{mm min}^{-1}$ , on the Zwick 250 UTM until full densification. Whereas in compression, the force and displacement were captured via the UTM extensometer, in tension the displacement was captured using 3D digital image correlation using a system by Correlated Solutions (Cameras: CSI-acA2440-75um, Lenses: Xenoplan 2.0/28-0901, Software: VIC-3D 9, Subset: 31, Step: 7). To facilitate statistical evaluation, a minimum of three replicates were conducted for each test.

The engineering stress,  $\sigma$ , was calculated as  $\sigma = F/A_0$ , where  $F$  is the reaction force, and  $A_0$  is the initial cross-sectional area of the specimens. The engineering strain,  $\epsilon$ , was calculated as  $\epsilon = \Delta l/l_0$ , where  $\Delta l$  is the elongation or contraction of the specimen's gauge length, and  $l_0$  is the initial gauge length of the specimen. The Young's modulus,  $E$ , was calculated within the elastic regime as  $E = \sigma/\epsilon$  and is a measure of resistance to deformation

of the material. The energy absorbed under compression,  $W$ , was obtained by integrating the stress–strain response of the bulk specimen. In the case of the cellular specimen,  $W$  was obtained by integrating the stress–strain curve up to the onset of densification, indicated by the densification strain,  $\epsilon_d$ , and calculates to  $W = \int_0^{\epsilon_d} \sigma(\epsilon) d\epsilon$ . Here, the densification strain was characterized as the initial point of densification within the material. This critical strain was identified by the intersection of tangents drawn to the stress plateau region and the densification region.<sup>[44]</sup>

Piezoresistive performance was measured using a Fluke 8846 A bench digital multimeter, offering a resistance range from 10  $\Omega$  to 1 G $\Omega$ . The specimens were suitably prepared by applying silver paste to the end of the gauge length to minimize contact resistance where a cable was connected to the multimeter. The samples were electrically insulated from the UTM by adding an extra layer of polypropylene tape between the sample and the grip. For cellular samples, the top and bottom surfaces were coated with silver paint to minimize contact resistance, and the cables were connected to the multimeter to record the change in electrical resistance,  $\Delta R/R_0$ , with  $\Delta R = R - R_0$ , where  $R$  is the electrical resistance measured for a certain strain value and  $R_0$  is the electrical resistance under no load. To quantify the initial piezoresistive sensitivity of the specimens, the gauge factor,  $k$ , was evaluated within the initial piezoresistive response of the specimen and was defined as

$$k = \frac{(\Delta R/R_0)}{\Delta \epsilon} \quad (1)$$

where  $\Delta R/R_0$  was measured over a strain interval of  $\Delta \epsilon$ . As PEEK/GNP5 has very low electrical conductivity, samples were treated with sulfuric acid (concentration  $\geq 95\%$ ) for 30 s, washed with acetone and distilled water, and dried before mechanical testing, exposing the conductive network of the fillers at the surface and allowing a conductive network to form with the electrode.

#### 2.4.2. Quasistatic Cyclic Compression Tests

Strain-controlled, quasistatic cyclic compression tests were undertaken, involving a strain amplitude of 3% across 500 cycles. Within the conventional stress–strain curve, one encounters a toe region that does not signify an intrinsic material property. Instead, it emerges as an anomaly due to the absorption of slack, as well as the orientation or positioning of the specimen.<sup>[45]</sup> To mitigate this effect, a considerable degree of compensation was achieved by establishing a minimum strain of 2%, consequently oscillating between strain levels of 3% and 5%. A loading rate of 2  $\text{mm min}^{-1}$  was selected, mirroring the quasistatic compression tests executed until densification. This led to a testing frequency of 1/18 Hz.

### 2.5. Biological Characterizations

Scaffolds prepared for biological characterization were subjected to an initial treatment using sulfuric acid (concentration  $\geq 95\%$ ), for 30 s, followed by acetone wash and immersion in distilled water, creating an etched surface, to enhance cell attachment and migration inside the scaffold pores. In vitro characterization

of the scaffolds was performed using a murine osteoblast precursor cell line (MC3T3-E1). MC3T3-E1 Subclone 4 cells (ATCC CRL-2593) were expanded until 80% confluency in cell culture medium, containing  $\alpha$ -minimal essential medium, 10% fetal bovine serum, and 1% penicillin–streptomycin, which provide the necessary growth factors for cell maturation and prevent pathogenic contamination.

Following sterilization in 70% ethanol, the scaffolds were transferred to nonadherent 24-well plates and flushed using a cell culture medium to remove air or residual ethanol inside the pores. Afterward, MC3T3-E1 cells were detached using trypsin-EDTA and a suspension was prepared. A cell count was performed, and the cells were seeded dropwise on the scaffolds with a constant seeding density of 2000 cells per scaffold. Separate sets of cultures were prepared and maintained in cell culture medium for 1, 7, and 14 days, containing two sets of technical and four sets of biological replicates. A separate culture was prepared over 14 days in an osteogenic medium, comprising cell culture media supplemented with  $50\ \mu\text{g mL}^{-1}$  ascorbic acid, 10 nM dexamethasone, and 10 mM  $\beta$ -glycerophosphate, that play an important role in the engagement of the MC3T3-E1 cells toward differentiation into mature osteoblasts. This culture set was utilized as a reference to observe the relative influence of the scaffolds in inducing cell differentiation, against an artificial osteogenic environment. Control cultures (2D controls) were prepared with cells seeded in tissue culture-treated 24-well plates and maintained in separate setups, containing both osteogenic and cell culture medium for the corresponding periods. Change of medium was performed twice a week through the duration of culture. MC3T3-E1 cell feedback, cultured in presence of the scaffolds, was monitored by testing for cell viability, cell proliferation, and ALP activity.

### 2.5.1. Cell Viability

Cell viability was assessed using Alamar Blue assay, in samples collected from the 2D controls and cultures on days 1, 7, and 14. The cells were incubated overnight in a 96-well plate, followed by the addition of 10  $\mu\text{L}$  of Alamar Blue solution to each well, resulting in a total sample volume of 100  $\mu\text{L}$ . Subsequently, the samples were further incubated for 2–6 h in the dark at 37 °C. Fluorescence was measured at an excitation wavelength of 520 nm and an emission range of 580–640 nm using a microplate reader (Promega GloMax Explorer Multimode Microplate Reader).

### 2.5.2. Cell Proliferation

Cell proliferation was analyzed through DNA quantification, using cell lysates from the cultures. Cell samples were collected and transferred into 2 mL microcentrifuge tubes, centrifuged at 3000 rpm for 3 min followed by resuspension of the pellet in cell culture media. The samples were then left standing briefly in  $-80\ ^\circ\text{C}$  to induce thermal shock for lysing the cell membrane, followed by defrosting and sonication for 15 min to extract the DNA. The DNA was then quantified using the Quant-IT PicoGreen dsDNA Assay kit. 30  $\mu\text{L}$  of sample was added to 70  $\mu\text{L}$  of diluted PicoGreen solution and 100  $\mu\text{L}$  of Tris-EDTA

buffer, in each well. Standards of the same volume were prepared, followed by incubation of both samples and standards in 96-well plates for 1 h. Fluorescence was then read at an excitation wavelength of 475 nm and emission range of 500–550 nm using a microplate reader (Promega GloMax Explorer Multimode Microplate Reader). A DNA standard curve was established with a concentration range of 0 to 1  $\mu\text{g mL}^{-1}$  and the DNA content present in the cell samples was quantified from the standard graph.

### 2.5.3. Alkaline Phosphatase Activity

ALP activity was quantified using the cell lysates prepared during DNA quantification. The assay was carried out in 96-well plates, containing 30 and 60  $\mu\text{L}$  of substrate solution (5 mM para-nitrophenyl phosphate). The samples were incubated in the dark for 3 h and then 20  $\mu\text{L}$  of stop solution (0.2 M NaOH and 0.2 M EDTA) was added to each well to terminate the reaction. A standard curve was prepared with para-nitrophenol concentrations ranging from 0 to 28 nmol. Absorbance of samples and standards was read at 405 nm using a microplate reader (Promega GloMax Explorer Multimode Microplate Reader). ALP activity of the samples was calculated from the para-nitrophenol concentration determined from the standard graph.

## 2.6. Micro- and Nanocharacterizations

Scanning electron microscopy (SEM) analysis was conducted using a Hitachi 8240 instrument, using an acceleration voltage of 10 kV. Cryogenically fractured samples of the 3D-printed bulk material from the parent composites were prepared. The sample preparation involved cooling them significantly through immersion in liquid nitrogen for  $\approx 5$  min. Subsequently, controlled fracturing was carried out to achieve pristine, brittle fracture surfaces, revealing the nanoreinforcements present at these surfaces. The SEM images, as displayed in **Figure 3**, consistently depicted a well-distributed arrangement of nanofillers across all samples. CNTs manifested as intertwined rod-like structures, intricately woven and effectively dispersed along the specimen surfaces. Similarly, GNPs presented as flat, gently curved forms embedded within the polymeric matrix. Notably, the PEEK/CNT2.5/GNP2.5 composite exhibited a balanced showcase of both fillers in terms of their presence and distribution.

Furthermore, SEM imaging of the cellular scaffolds (**Figure 4**) validated the successful realization of the intended microstructures through the printing process. The images also unveiled the presence of surface pores on the extruded beads, a consequence of the FFF process. This surface irregularity introduced the possibility of affecting the mechanical and piezoresistive performance of the scaffolds when subjected to mechanical strains. The extrusion width at the points where two intersecting beads cross each other was noticeably expanded, due to the enhanced material accumulation in these locations. Since the material lacked support during its deposition atop the gaps between the beads, it underwent a slight settling effect through the printing process, leading to a reduction in its extrusion width. This phenomenon was attributed to the deliberate design choice and was fully intentional.

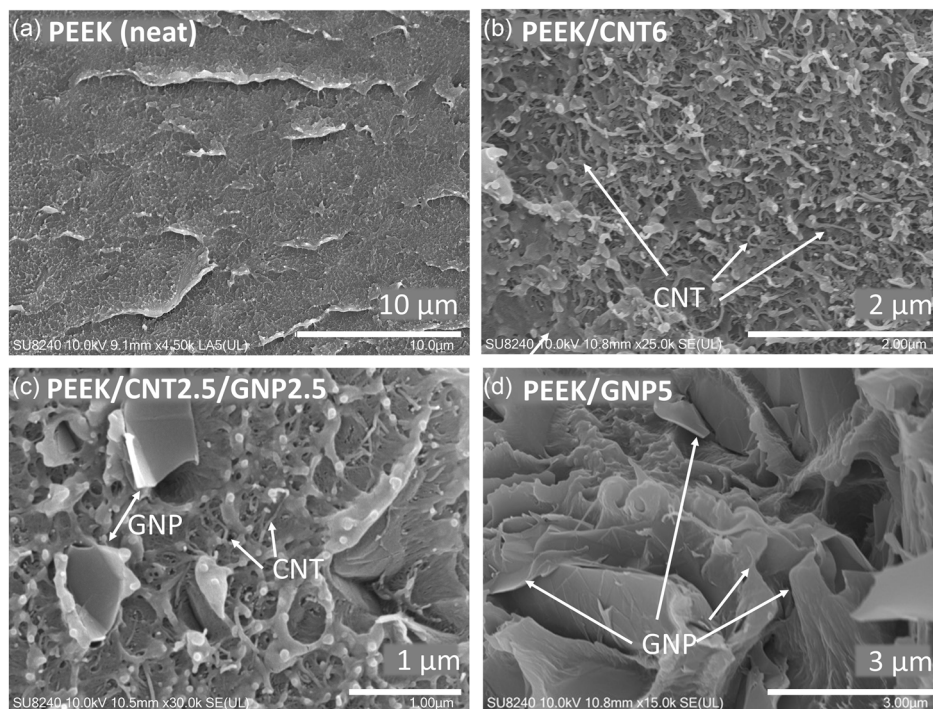


**Figure 3.** SEM images of cryogenically fractured surfaces of the parent composites studied: a) PEEK (neat), b) PEEK/CNT6, c) PEEK/CNT2.5/GNP2.5, and d) PEEK/GNP5.

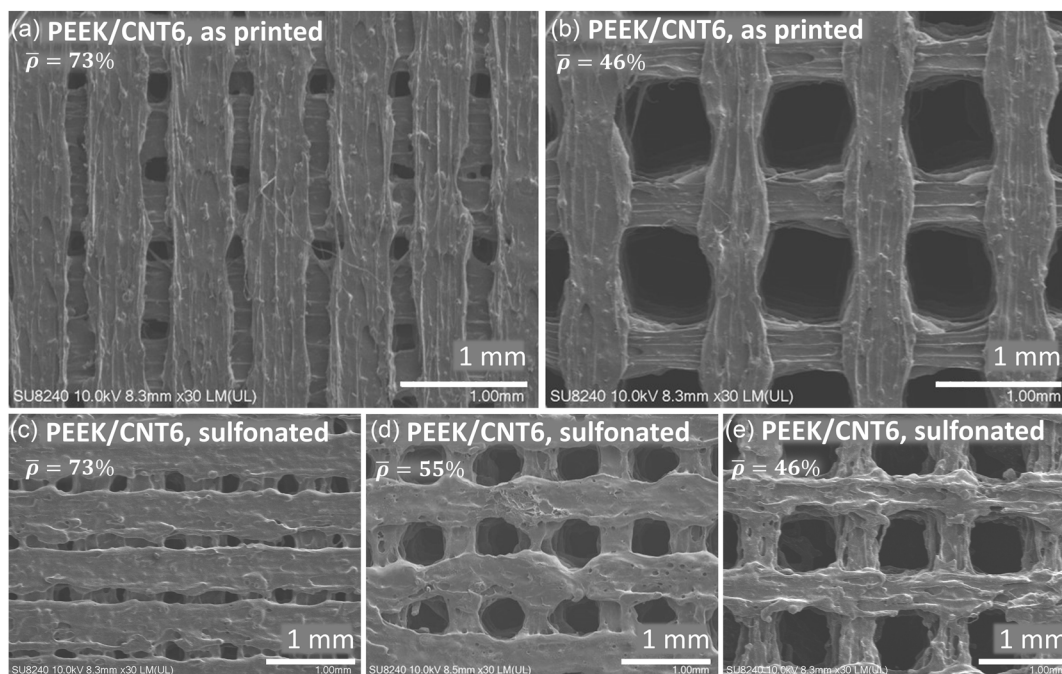


**Figure 4.** SEM images of PEEK/CNT6 scaffolds in a,b) as printed condition and c–e) in sulfonated condition at various relative densities.

Additional analyses, encompassing Fourier-transform infrared (FTIR) spectroscopy, X-ray diffraction (XRD), and differential scanning calorimetry (DSC), were conducted on PEEK and PEEK nanocomposites to characterize the parent

materials utilized in this study. Detailed discussions of these analyses are provided in the Supporting Information, including Figure S4 and S5, and Table S1 (Supporting Information).

### 3. Results and Discussion

This section describes and discusses the mechanical, piezoresistive, and biological performances of both bulk and cellular nanocomposites.

#### 3.1. Mechanical and Piezoresistive Performance of Parent Nanocomposites

Bulk samples for tensile and compression tests were fabricated using the FFF 3D printing technique. During the printing process at high temperatures above 400 °C and with 100% infill density, residual stresses were induced in the material which occasionally led to warping and delamination between layers. These challenges are associated with the solidification process of the polymer, affecting the interfacial adhesion between the beads.<sup>[26]</sup> Despite these issues, most of the samples exhibited good dimensional accuracy. To minimize the warping, a two-layer raft was introduced, printed in ±45° direction with 50% infill, which effectively reduced mechanical stresses between the build plate and the sample surface, resulting in improved and more consistent prints. However, it should be acknowledged that high crystallinity and high shrinkage coefficients affect the dimensional stability of the part, particularly when processing semicrystalline polymers such as PEEK.<sup>[26]</sup>

One of the critical factors influencing print quality was found to be the varying diameter of the filament feedstocks. Analysis revealed that the diameter of the custom-made filaments varied more than what is typically observed for commercially available filaments, which usually have a diameter of 1.75 ± 0.05 mm. Measurements using an in-line filament measurement setup (Filameasure and Filalogger from Filabot) confirm variations in filament diameters for PEEK (neat), PEEK/CNT6, PEEK/CNT2.5/GNP2.5, and PEEK/GNP5 with 1.72 ± 0.07, 1.84 ± 0.07, 1.76 ± 0.11, and 1.77 ± 0.09 mm, respectively (see Supporting Information, Figure S3). The inconsistency in filament diameter warrants changes to the process parameters, necessitating adjustments to the extrusion multiplier handle to achieve optimum results. This can sometimes lead to underextrusion and unwanted process-induced interbead and intra-bead multiscale voids in the as-printed structures, especially in areas with thinner sections of the filament encountered during the printing process. Consequently, the printed PEEK nanocomposites, although exhibiting enhanced stiffness due to CNT reinforcements, still show reduced strength and toughness as summarized in **Table 1**. It is crucial to highlight that the central objective of this study is to introduce a sensing attribute to PEEK. It should be noted that the optimization of filament extrusion and the 3D

printing processes are not within the current scope of this investigation.

It is worth noting that PEEK (neat) exhibits excellent performance under tensile loading, with stiffness and strength close to that of injection-molded parts.<sup>[26]</sup> For composites comprising CNTs or GNPs, a significant increase in stiffness is observed in all cases, up to 5.1 GPa for PEEK/CNT2.5/GNP2.5, while at the same time, the standard error for replicates increases due to the aforementioned challenges. Importantly, the introduction of fillers can result in a reduction in strain tolerance of the PEEK composites. In addition, the increased crystallinity resulting from the presence of fillers combined with the process-induced changes due to the presence of fillers can also contribute to a decrease in strain tolerance (ductility), further affecting the mechanical performance of the resulting PEEK nanocomposites.<sup>[35]</sup> The multiscale porosity induced by printing process further reduces the strength, leading to early failure, and in some cases, the maximum strength achieved is below that of the neat polymer. As a result, the elongation at break of the nanocomposites is lower than that of the neat PEEK.

The density of MWCNTs is around 1.74 g cm<sup>-3</sup>,<sup>[46]</sup> that of GNP around 2.2 g cm<sup>-3</sup>, while that of PEEK (neat) is reported to be around 1.3 g cm<sup>-3</sup>.<sup>[47]</sup> Density calculations of 3D printed bulk samples with a dimension of 10 × 10 × 10 mm<sup>3</sup> were performed to assess the porosity induced by the printing process. The results indicate that the porosity of 3D-printed PEEK is around 3.1%, while that of PEEK/CNT6, PEEK/CNG2.5/GNP2.5, and PEEK/GNP5 composites is higher with 9.7%, 5.1%, and 8.7%, respectively. Consequently, the density of the PEEK composites was found to be lower than that of PEEK (neat) (Table 1), contrary to what would be expected due to the higher density of the filler material compared to the neat PEEK.

The strain sensitivity of the samples was assessed and quantified via the gauge factor (Equation (1)) and was evaluated to be higher for PEEK/CNT6 compared to PEEK/CNT2.5/GNP2.5 (Table 1). PEEK/GNP5 specimen did not show appreciable change in resistance due to its higher zero-load resistance ≈ 1 GΩ; hence, no gauge factor could be calculated. This indicates that the GNP-filled PEEK composites have a much higher electrical percolation threshold than CNT PEEK composites, which is consistent with other studies, reported on nanoreinforced composites prepared in a similar manner.<sup>[39,48–50]</sup>

#### 3.2. Mechanical and Piezoresistive Performance of Cellular Nanocomposites

Cellular structures of PEEK and PEEK nanocomposites were 3D printed and subjected to compressive loading, allowing for the assessment of their mechanical and piezoresistive responses

**Table 1.** Summary of tensile properties of PEEK and PEEK nanocomposites.

Material	Young's modulus [MPa]	Tensile strength [MPa]	Elongation at break [%]	Energy absorbed [MJ m <sup>-3</sup> ]	Gauge factor [-]	Density [g cm <sup>-3</sup> ]
PEEK (neat)	3490 ± 37	88.3 ± 16.6	9.3 ± 3.4	4.8 ± 2.4	–	1.26
PEEK/CNT6	4154 ± 749	76.8 ± 12	4.8 ± 1.8	2.79 ± 1.43	7.3 ± 10	1.20
PEEK/CNT2.5/GNP2.5	5054 ± 646	74 ± 13	1.61 ± 0.5	1.1 ± 0.7	2.8 ± 1.3	1.27
PEEK/GNP5	4907 ± 78	58.4 ± 11.6	1.8 ± 0.3	0.67 ± 0.29	–	1.23



as a function of strain, considering various combinations of CNTs and GNPs as well as the relative densities.

**Figure 5** presents the stress–strain response and corresponding change in the normalized resistance of the cellular structures. The graphs clearly illustrate three distinct regimes, linear elastic, plastic, and densification, for different relative densities of 46%, 55%, and 73%, separately. Initially, all structures demonstrate a linear increase in stress until reaching their yield point, where the stiffness decreases, resulting in a flattening stress curve. Subsequently, a local stress peak is observed, followed by failure of the ligaments, causing the stress to decrease before reaching the point of densification. Densification is observed at  $\approx 50\%$ – $70\%$  strain. Interestingly, for cellular structures with high relative density, a continuous increase in stress up to full densification is observed, with no apparent local maxima or stress drop.

**Figure 6** illustrates the corresponding mechanical and piezoresistive characteristics of the cellular structures obtained from experiments under compressive loading, each corresponding to its respective relative density, with the absolute values summarized in Table S3 (Supporting Information). As expected, an increase in relative density leads to an increase in Young's modulus, strength, and energy absorption. This is evident for PEEK (neat), PEEK/CNT2.5/GNP2.5, and PEEK/GNP5. However, for PEEK/CNT6, some challenges were encountered due to manufacturing-related issues associated with the quality of the feedstock, as discussed for bulk materials. Additionally, the high filler content posed difficulties during 3D printing, leading to occasional partial clogging of the printer nozzle, resulting in temporarily reduced material deposition and consequently reduction in performance.

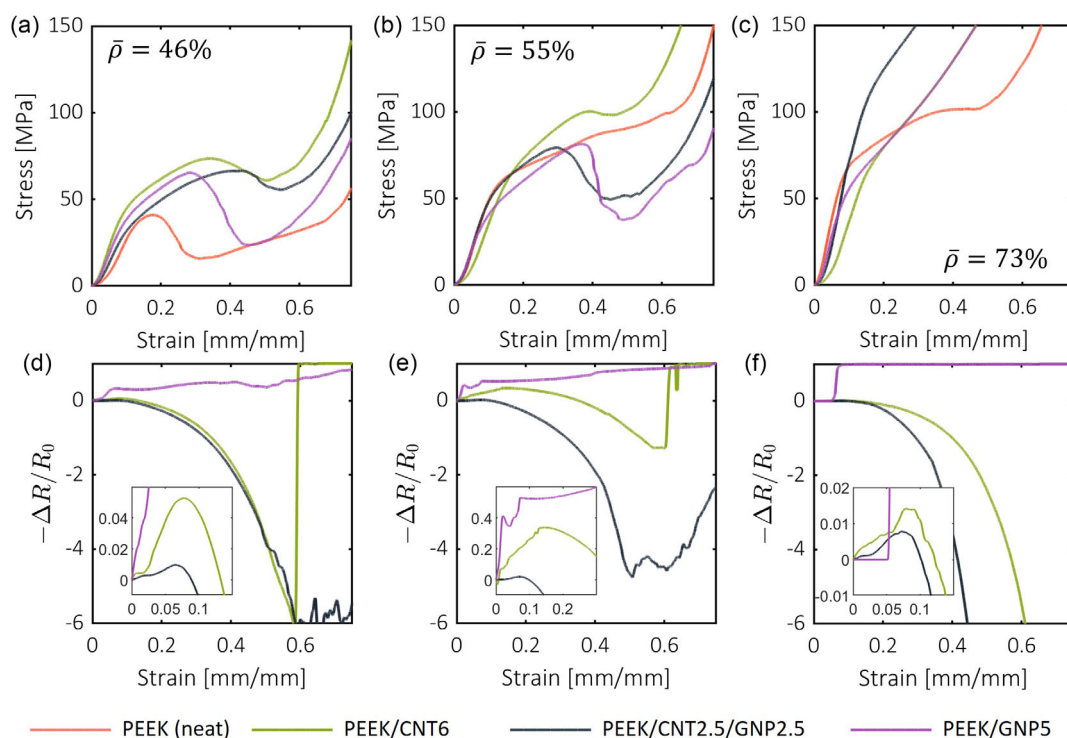


**Figure 5.** Cellular structures under compressive loading: a–c) representative stress–strain response and d–f) corresponding normalized change in resistance as a function of strain.

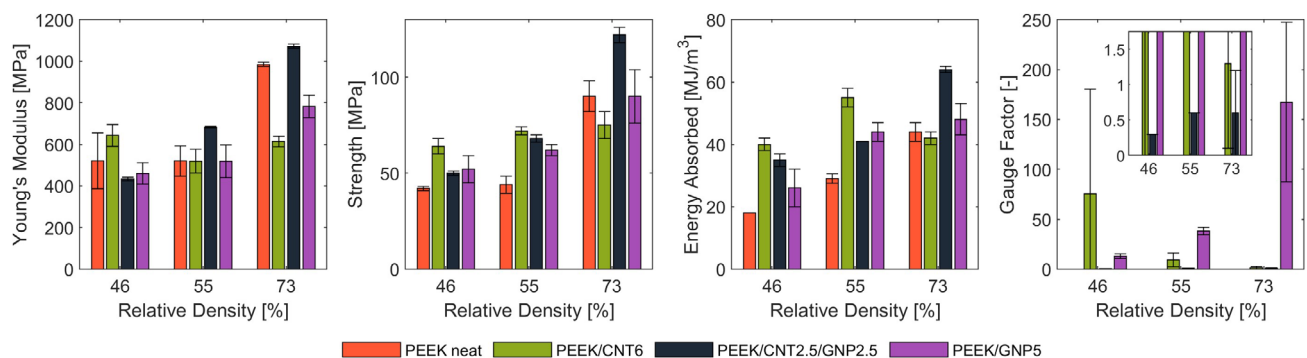


**Figure 6.** Mechanical and piezoresistive performance characteristics for cellular structures under quasistatic compression loading.

The PEEK/CNT2.5/GNP2.5 scaffolds at 73% relative density exhibited the highest levels of stiffness, strength, and energy absorption among the tested materials. PEEK (neat) also performed exceptionally well despite lacking any reinforcing fillers, owing to its excellent print quality. With the decrease in relative density, PEEK/GNP5 exhibited a mechanical response similar to PEEK/CNT2.5/GNP2.5, although it tended to experience slightly earlier failure, resulting in lower energy absorption in most cases. On the other hand, PEEK/CNT6 lattices underperformed due to reduced print quality at higher relative density. Interestingly, PEEK/CNT6 performs excellently with the lowest relative density, making it the best composite explored here.

The change in normalized resistance as a function of strain exhibits very clear trends under compressive loading, which correspond well with the stress–strain responses. Three distinct general trends were observed, reflecting the choice of nanofillers. In the case of PEEK/CNT6, there is an initial decrease in the change of electrical resistance (note that the change in resistance, as shown in Figure 5, is plotted as  $-\Delta R/R_0$ ) occurring within the linear elastic regime until the material yields. The increase in conductivity is expected due to the creation of new electrical pathways as the material is elastically compressed, allowing more electrons to travel uninterrupted through the lattice. The gauge factor reaches values of up to  $\approx k = 75$  (PEEK/CNT6 at 46% relative density). With an increase in relative density, the gauge factor decreases due to a decrease in change in resistance of the cell wall material, implying a reduced sensitivity of the material to changes in strain. As the material yields and continues to reach its stress peak under compressive loading, the lattice permanently deforms and slowly breaks apart. This can be observed visually by the reduction in the stress at lower relative densities and the increase in stress at higher relative densities at elevated strains. As a result, conductivity decreases, and the resistance change increases smoothly and consistently with approximately exponential growth up to a maximum point where the cellular material begins to densify, typically occurring at a strain between 50% and 60%. During this phase of plastic deformation and damage, the conductive pathways within the polymer matrix are significantly disrupted. The CNTs lose contact with each other, and the distance between the CNTs increases, diminishing the tunneling effect. With further compression and the onset of densification, the change in resistance levels out due to the percolation of new contacts due to folds forming between the cell walls within the scaffold under compression, and in some cases, a sudden jump is observed, revealing a complete conductive response. This jump occurs due to the contact between the silver coating on the top and bottom surfaces, creating a fully conductive path for electrons to travel freely. At this stage, the response no longer accurately reflects the material's behavior, but such observations are not necessary as the structure no longer serves a scientific purpose given the extent of deformation.

Distinct trends were observed for PEEK/GNP5 composites. Despite having 5 wt% GNP within the polymeric matrix, the percolation threshold had not yet been reached. To remove the polymer layer covering the nanofillers on the surface, the samples underwent treatment with sulfuric acid for 30 s, followed by consecutive treatment with acetone and distilled water to eliminate any remaining acid residue. This procedure facilitated the exposure of the conductive network on the sample's surface, resulting

in resistance readings several orders of magnitude higher than those measured for PEEK/CNT6. In most instances, an initial steep decrease in the change of resistance is noted under compression. This reduction flattens out and gradually approaches a value of 1 for a fully conductive material in a linear manner. The ongoing increase in conductivity can be attributed to the collapsing of cell walls onto each other. This process continuously increases the exposed surface area, allowing more electrons to traverse the lattice's surface until densification occurs. At this stage, the scaffold becomes fully conductive due to contact between the top and bottom surfaces coated with silver paint. Because of the distinct mechanism employed to establish an electrically conductive network, the response of the change in resistance as a function of strain exhibits a less smooth appearance, rendering the material more susceptible to surface cracking. Interestingly, in contrast to PEEK/CNT6, this leads to a higher gauge factor in the elastic region for high relative densities, with the factor increasing as relative density reduces due to the corresponding increase in the sample's surface area. With PEEK/CNT2.5/GNP2.5, similar observations were made as for PEEK/CNT6 although the change in resistance within the linear elastic range was observed to be small with the gauge factor for all relative densities observed being consistently lower than one. However, after the material yields, the resistance change follows the same trend as previously described for PEEK/CNT6 composites.

In addition to the compression tests up to densification, the scaffolds also underwent quasistatic cyclic compressive loading, featuring a strain amplitude of 3%, a maximum strain of 5%, a strain rate of  $0.0033 \text{ s}^{-1}$ , and testing frequency of 1/18 Hz (cycles per second) within the elastic regime. Only cellular scaffolds with a 55% relative density were tested here to maintain the experiment within a reasonable scope. This cyclic loading was applied for over 500 cycles, with the results displayed in Figure 7 for selected cycles (3, 10, 100, 300, and 500). In contrast to metals, the fatigue behavior of polymeric materials like PEEK is notably influenced by their intrinsic viscoelastic properties, which are dependent on time and frequency. At elevated frequencies, there is a potential for PEEK to undergo softening and melting, leading to accelerated fatigue failure due to thermal softening. In this study, the loading rate and consequently the frequency were set significantly low to prevent any heating of the scaffolds during the loading process.<sup>[51]</sup>

The stress–strain plots exhibit a nearly linear stress increase during the loading process, reaching a maximum at 5% strain, followed by stress reduction back to 2% strain. This hysteresis loop, depicting the energy dissipation during each load–unload cycle, becomes smaller as the number of cycles progresses due to irreversible microscale fractures within the lattice. The area within the loop indicates the energy dissipation: the area decreases with increase in number of cycles, signifying that the energy dissipated per cycle decreases and reaches a saturated value. If the maximum strain imposed would exceed the yield strain, the dissipation would be attributed to inelastic processes such as (viscous) plasticity and damage. Conversely, as the maximum imposed strain is lower than the yield strain, the dissipation is due to viscoelastic energy dissipation combined with microscale fractures. Consequently, an anticipated decrease in maximum strength at 5% strain occurs with an increasing

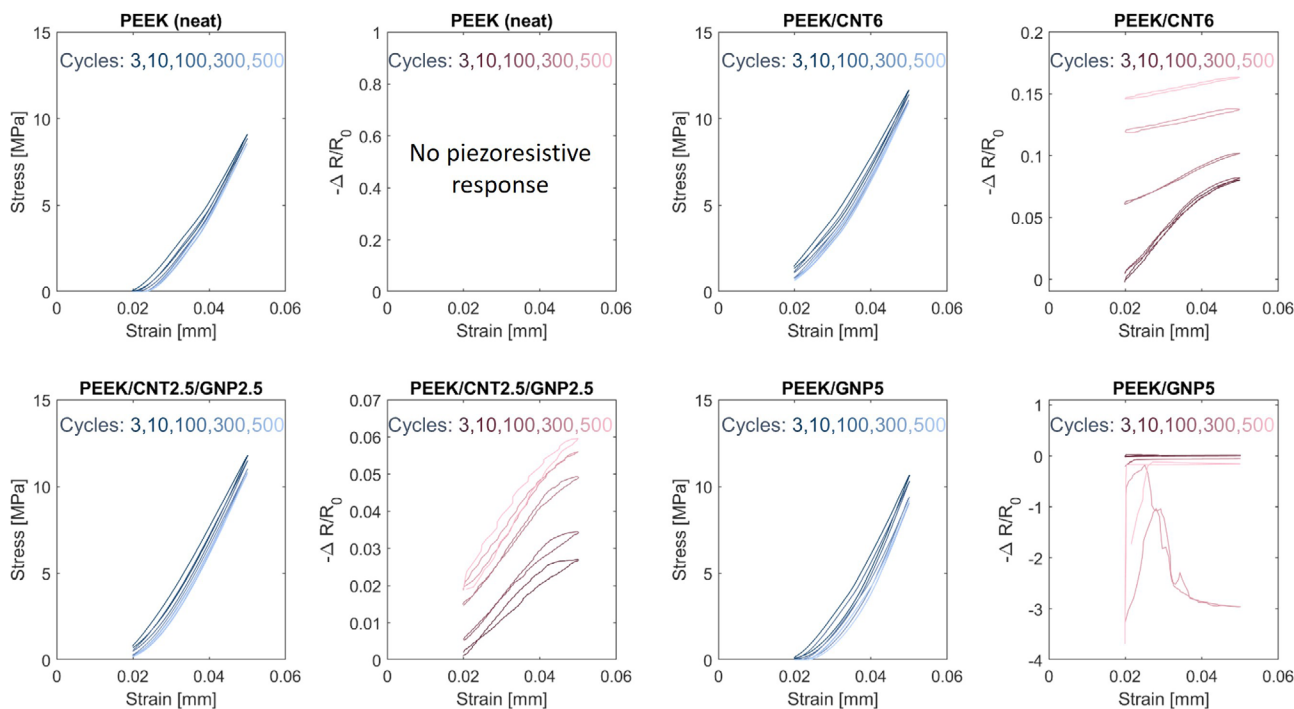


**Figure 7.** A representative stress–strain response and change in resistance versus strain is shown for all materials tested under quasistatic cyclic compressive loading for selected cycles of 3, 10, 100, 300, and 500 ( $\bar{p} = 55\%$ ).

number of cycles. This decline slows significantly as the number of cycles increases.

Concurrently, data was gathered on the alteration in electrical resistance concerning strain and cycles, illustrating the hysteresis loops of the loading and unloading cycles in Figure 7 for a chosen set of cycles (3, 10, 100, 300, and 500). Initially, there is a decrease in resistance change as strain escalates. This reduction tapers as the strain reaches its zenith of 5%, marking the conclusion of the loading cycle. During unloading, the resistance alteration follows a trajectory similar to the loading process. However, the residual resistance at the end of the unloading cycle experiences a marginal decrease compared to the preceding cycle, implying a minor but permanent alteration in the electrically conductive structure. While the amplitude of the change in resistance remains relatively constant for PEEK/CNT2.5/GNP2.5 composites across all tested cycles, it steadily diminishes with escalating cycle numbers for PEEK/CNT6. This hints at a gradual decline in material sensitivity as cycles accumulate, albeit the rate of this reduction considerably decelerates over prolonged testing periods.

A distinct trend emerged for PEEK/GNP5, as anticipated due to the material's generally low conductivity, necessitating surface etching for assessment. Similarly, the variation in resistivity decreases with increasing strain until a peak is reached, subsequently leaving the residual change in resistivity slightly below the initial cycle's level. As a result, successive cycles exhibit lower resistivity compared to their predecessors. Notably, anomalies arise with progressive cyclic compression, particularly beyond  $\approx 200$  cycles. These anomalies entail unexpected resistance signal spikes, leading to erratic cyclic performance thereafter. This

phenomenon is attributed to an unstable conductive network on the sample surfaces, which becomes disrupted during higher loading intervals. Beyond this threshold, hysteresis loops fail to provide meaningful insights due to the complexities involved.

To provide additional validation for these observations, hysteresis analysis was performed. Figure 8 displays stress peaks, resistance at maximum and minimum imposed strains, mean slope, and energy dissipation as functions of cycle number. The mean slope in this case was calculated as the average slope of the loading and unloading cycles of the stress–strain response. These results affirm a decrease in the load-bearing capacity known as cyclic softening by an average of  $11.4 \pm 0.7\%$  across 500 cycles and signify the phenomenon of polymer chain relaxation.<sup>[52]</sup> Notably, for PEEK/CNT6 and PEEK/CNT2.5/GNP2.5, a clear correlation emerges between the decline in electrical resistance peaks and the concurrent reduction in mechanical response over time. In contrast, for PEEK/GNP5, an inverse pattern emerges, with irregularities becoming apparent starting around cycle 200. Here, a significant increase in the amplitude of the normalized resistance peaks occurs after 200 cycles, indicating a significant disruption of the conductive network with a higher cycle number.

The energy dissipation for all materials during the loading cycles exhibits a significant decrease of  $90 \pm 3\%$  over 500 cycles, with the primary reduction occurring during the initial cycles. This suggests that after a low number of cycles, the scaffolds reach a stable state in which the energy dissipation becomes very low, and the scaffolds fully manifest their potential. The mean slope as a function of cycle decreases with prolonged testing, as expected, although fluctuations are present, the overall trend

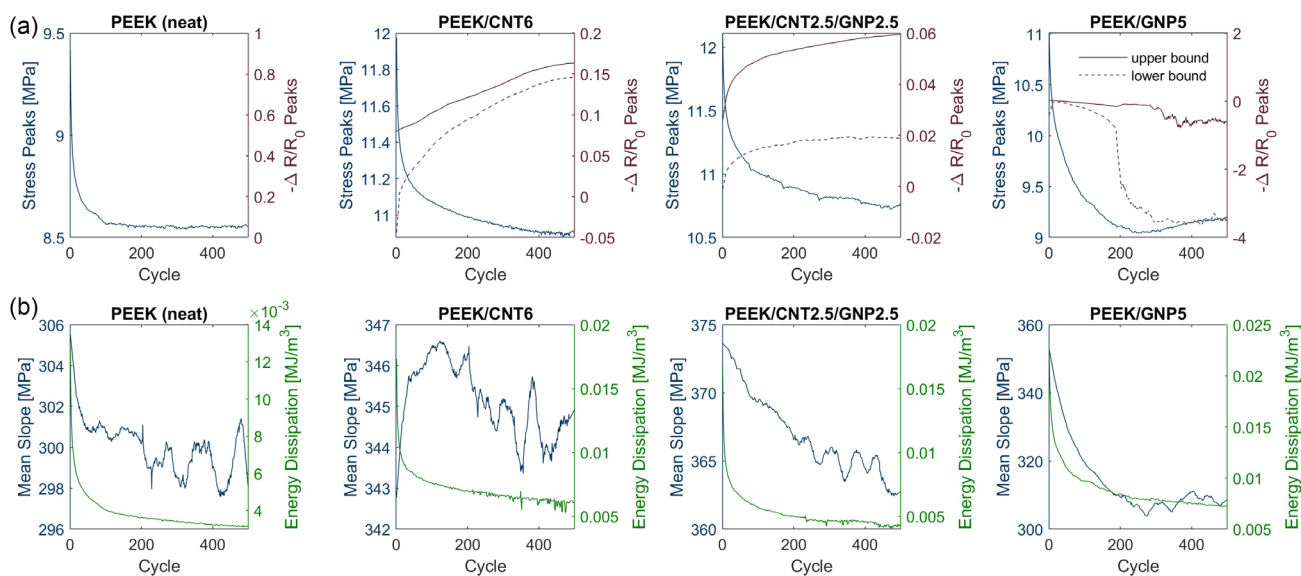


**Figure 8.** Scaffolds of  $\bar{\rho} = 55\%$  under compressive loading: a) Representative stress peaks versus number of cycles and variation in resistance peaks (at maximum and minimum strain levels) versus number of cycles are shown for all materials tested. b) Representative mean slope and energy dissipation as a function of number of cycles.

is clear. This indicates a reduction in stiffness with prolonged testing. Interestingly, during cyclic loading, the mean slope of all composites was observed to be significantly higher than that of neat PEEK, signifying the reinforcing effect of the nanofillers used in the composites.

### 3.3. Biological Characterization of Scaffolds

#### 3.3.1. Cell Viability

Cell viability is assessed through Alamar Blue assay, which uses a blue indicator dye, Alamar Blue or resazurin. Metabolically active cells can take up resazurin and reduce it into a highly fluorescent pink product, resorufin. With progressive reduction of resazurin and increasing concentration of resorufin, the fluorescence of the medium increases, which is recorded through the microplate reader. A higher fluorescence value represents a higher proportion of metabolically active or viable cells in the medium, thus pointing to the cytocompatibility of the architected scaffold. The results obtained over 14 days of cultured MC3T3-E1 cells as well as the 2D controls are shown in **Figure 9**.

The results for cell viability of the scaffolds are assessed against the 2D controls as well as the cultures prepared as a reference, in osteogenic media over 14 days (see Supporting Information, Figure S6). Comparing the results, throughout the culture period, it can be observed that the percentage viability of cells increases between days 1 and 7. Cell survival and metabolism show a positive trend, across the culture period. Composites of PEEK/CNT6 with relative densities of 46% and 73% as well as PEEK/GNP5 with a relative density of 73% show rapid increases in their cell viability by day 14. Scaffolds of PEEK/GNP5 having lower relative densities show relatively low cell survival. Assays performed upon cells grown in osteogenic media reveal peaks of percentage cell viability at 90% to 100%,

comparable to the 2D controls, in scaffolds of PEEK/CNT2.5/GNP2.5, of all relative densities, while much lower cell viability is observed in scaffolds of all other materials and geometries. Cells cultured on PEEK/CNT2.5/GNP2.5 scaffolds, along with additional osteogenic components in the media, show a considerably higher metabolic response. The characteristic flattening of the percentage viability after reaching a peak can indicate the beginning of a stationary phase of cell growth or the commitment of the MC3T3-E1 precursors toward the osteoblastic lineage, following the active growth phase, resulting in lower metabolic activity during differentiation into mature osteoblasts.

#### 3.3.2. Cell Proliferation

Cell proliferation is determined by quantifying the concentration of DNA across 14 days of cell culture, on the scaffolds as well as the 2D controls. As demonstrated in **Figure 10**, on day 1, all the scaffolds show relatively low and consistent concentrations of DNA for each material and relative density, followed by a steady rise by day 7 and a general decline by day 14. Although cells proliferated in the presence of all the materials and geometries, the DNA content observed in the 2D controls is considerably higher than that in the presence of the scaffolds on day 14. Maximum overall proliferation can be observed on day 7, where higher rates of cell multiplication are seen in the scaffolds compared to the 2D controls. However, distinct patterns in proliferation are observed, specific to the scaffold material and its relative density, and these parameters exert an apparent influence on the rates of cell division for each scaffold. PEEK neat scaffolds show a relatively slow increase through days 1 and 7, followed by a constant DNA content on day 14. Cell multiplication shows little increase in PEEK neat scaffolds through the culture period, though the neat PEEK scaffolds with 46% relative density show a similar decline. Comparing the nanocomposites, highly pronounced cell

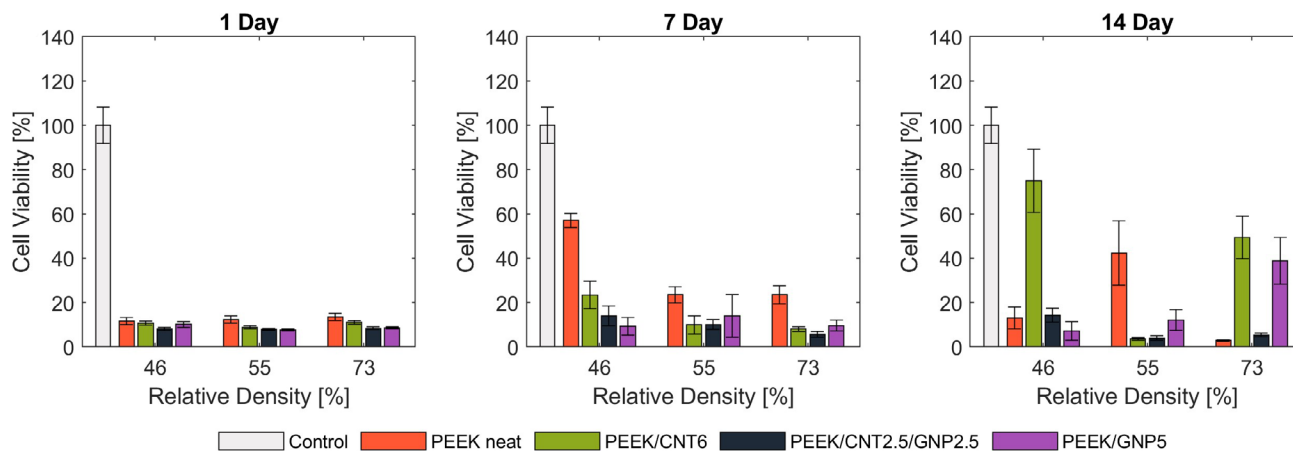


**Figure 9.** MC3T3-E1 cell metabolic activity determined from Alamar Blue assay results, denoting the percentage viability of cells across 14 days of culture.

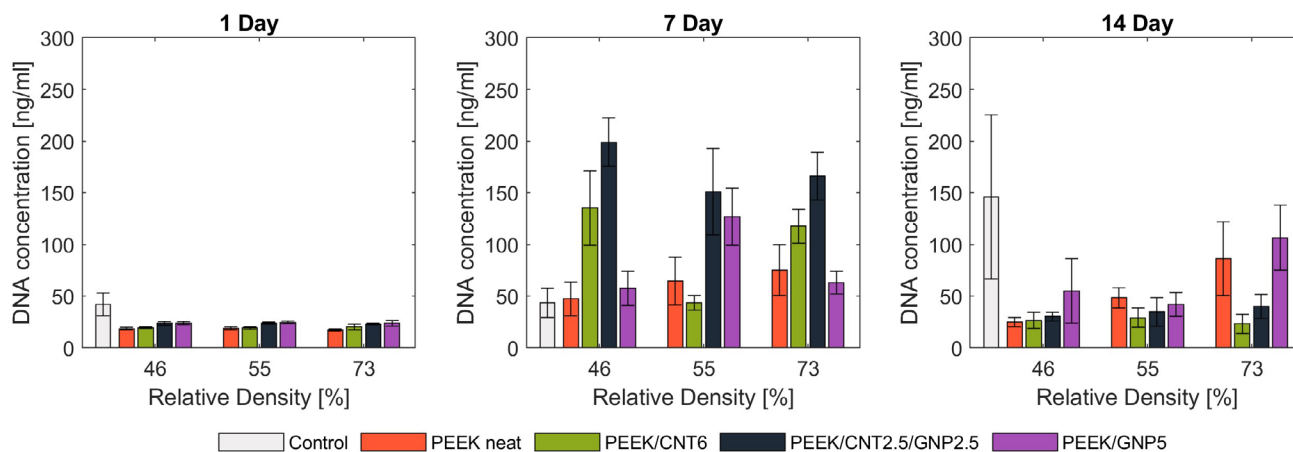


**Figure 10.** Cell proliferation rates determined from DNA concentration, measured over 14 days of culture.

proliferation is seen, with DNA concentrations of around  $200 \text{ ng mL}^{-1}$ , in scaffolds, having relative densities of 46% and 73% made of PEEK/CNT6 and PEEK/CNT2.5/GNP2.5, on day 7. PEEK/GNP5, of relative densities 55% and 73%, exhibits a similar profile, showing DNA concentration peaks at around  $150 \text{ ng mL}^{-1}$  on day 7 and  $120 \text{ ng mL}^{-1}$  on day 14, respectively. Cells cultured in osteogenic media, in the presence of PEEK/CNT2.5/GNP2.5 scaffolds, of all relative densities, show high concentrations of DNA, between  $150$  and  $200 \text{ ng mL}^{-1}$ , comparable to or surpassing that of the 2D controls.

### 3.3.3. Alkaline Phosphatase Activity

ALP activity was quantified, using ALP enzyme as a phenotypic marker, that assessed the influence of the scaffolds toward engaging cells for differentiation into mature osteoblasts. Enzyme activity was determined by recording the absorbance of para-nitrophenol, produced through an ALP-driven reaction with para-nitrophenyl phosphate. ALP expression can be observed throughout the span of cell culture and differentiation is sustained by all scaffolds tested. The overall ALP activity of

the scaffolds increases exponentially through days 1 to 7 and remains relatively constant until day 14. On day 1, initial enzyme expression of all scaffolds is negligible compared to that of the 2D controls, followed by elevated expression within the rest of the culture period. This may be indicative of the influence, exerted by the scaffolds, on the cells, toward differentiation in the osteoblastic lineage, upon successful cell survival and proliferation.

ALP concentrations in samples of PEEK/CNT2.5/GNP2.5 of relative density 46%, show the highest peak on day 7. The general expression of ALP is consistent with the response of the material in the cell viability and proliferation assays. While all structures can be considered conducive for cell differentiation in vitro, scaffolds of neat PEEK and PEEK/CNT2.5/GNP2.5 with relative densities of 46% and 73%, respectively, exhibit a comparatively higher extent of MC3T3-E1 differentiation, proportional to the levels of expressed ALP. Scaffolds of PEEK/CNT2.5/GNP2.5, tested in the presence of osteogenic media, show higher expressions of ALP, at around  $6 \text{ U/mL}$ , than in results observed in **Figure 11**, where maximum ALP expressed in the corresponding samples amounts to  $4\text{--}5 \text{ U/mL}$  at the end of the cell culture period, on day 14.

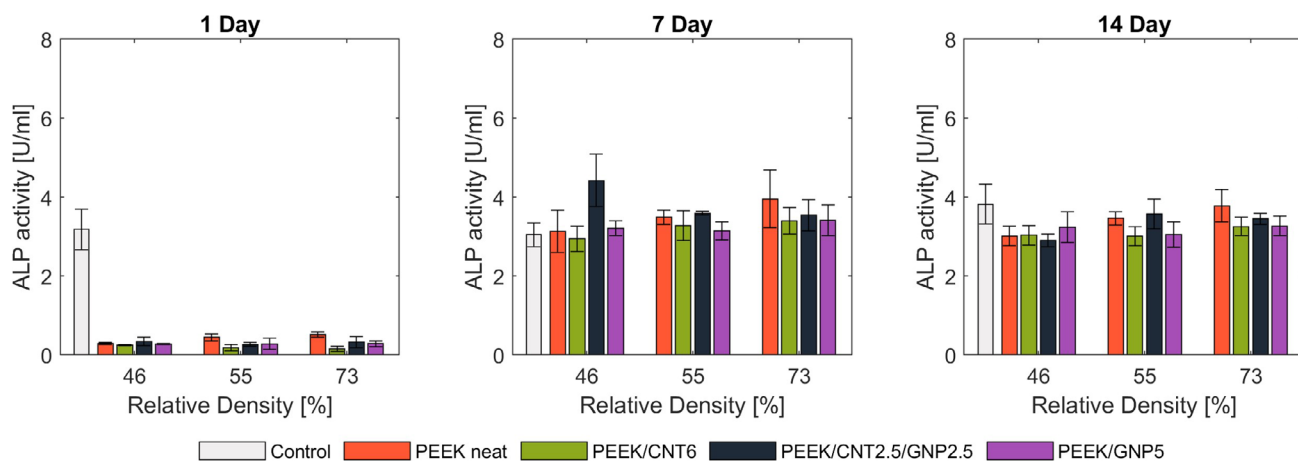


**Figure 11.** Results for ALP enzyme expression mapped across the 14-day cell culture span.

## 4. Conclusion

In this study, mechanical, piezoresistive self-sensing, and biological characteristics of 3D-printed PEEK smart polymer nanocomposite scaffolds were experimentally investigated. Scaffolds composed of PEEK/CNT 6 wt% exhibited a gauge factor of 75, Young's modulus of 0.64 GPa, and a strength of 64 MPa, all at a relative density of 46%. In contrast, scaffolds comprising PEEK/CNT2.5/GNP2.5 achieved a modulus as high as 1.1 GPa and a strength of 122 MPa, exhibiting remarkable mechanical properties, at a relative density of 73%. The integration of XRD, DSC, and FTIR spectroscopy analyses offers a comprehensive understanding of the structural, thermal, and molecular characteristics of the PEEK composites. The piezoresistive response exhibited three distinct trends contingent on the nano-filler content and relative density of the scaffold. High sensitivity was evident within the elastic regime for low relative density scaffolds made of PEEK/CNT6 composites. However, this sensitivity lessened as the CNT content was reduced and supplanted by GNPs. Concomitant with material yielding, observable peaks in resistance alterations occurred. These characteristics facilitate the determination of the strain state and furnish insights into whether the deformation is reversible or permanent. The notable piezoresistive response to induced strains in the plastic regime of PEEK/CNT6 and PEEK/CNT2.5/GNP2.5 composite scaffolds under compressive loading signifies their strong potential for utilization in strain and damage-sensing applications. The resilient mechanical and piezoresistive responses of both PEEK/CNT6 and PEEK/CNT2.5/GNP2.5 scaffolds under cyclic compression (500 cycles) over a small strain range indicate the sensors' suitability for extended use.

Biological analysis of the scaffolds reveals sustained cell survival in all samples, with prominent percentages of viable cells observed in scaffolds of PEEK/CNT6 of relative density 46%, pointing to its superior ability of cell maintenance. PEEK/CNT6 scaffolds continue to exhibit dominant trends in cell proliferation and a consistently elevated ALP expression. This suggests consistent compatibility of bone cell precursors influenced by scaffolds of this material and its potential to further be assessed and functionalized for bone tissue engineering in

routine medical utilization. Remarkable cell response observed from cultures on PEEK/CNT2.5/GNP2.5 scaffolds, in the presence of osteogenic media, suggests their enhanced performance, upon the addition of differentiation factors, compared to that in culture media. They exhibit a cell viability of 90%–100% and a consistently high ALP activity of 5 to 6 U mL<sup>-1</sup>. This can indicate the necessity of supplementary osteogenic growth factors and functionalization with bioactive fillers or coatings for this material, to accelerate recovery at the implant site, during utilization in vivo. Variable responses of cell metabolism observed for each scaffold point to the selective affinity of cells toward a specific material and geometry. Uniformity in ALP expression throughout the culture period suggests successful engagement of the MC3T3-E1 precursors for differentiation into mature osteoblasts. The growth and metabolic activities of cells can be affected by factors such as variations in surface roughness within the scaffold architecture, arising from uneven extrusion rates during fabrication or inconsistencies in the dispersion of nanofillers.

Both PEEK/CNT6 and PEEK/CNT2.5/GNP2.5 exhibit a high potential for application as smart materials in engineered bone implants. While the biological results provide evidence for the efficacy of the scaffolds in an in vitro environment, conclusive insights can further be obtained by exploring analytical techniques, enabling real-time visualization of biological feedback in the presence of the scaffolds and prediction of their effectiveness in vivo. Further investigations encompassing a broader range of PEEK nanocomposites, scaffold topologies, and biological conditions are necessary to identify PEEK nanocomposite scaffolds with optimal performance. Finite-element studies, aimed at forecasting both mechanical and piezoresistive performance, to establish a predictive capability, are currently under exploration but have been deferred for further study.

## Supporting Information

Supporting Information is available from the Wiley Online Library or from the author.

## Acknowledgements

This work was supported in part by the EPSRC Centre, funded by the UK Engineering and Physical Sciences Research Council (grant EP/R513222/1) and the University of Glasgow.

## Conflict of Interest

The authors declare no conflict of interest.

## Data Availability Statement

The data that support the findings of this study are available from the corresponding author upon reasonable request.

## Keywords

additive manufacturing, bone tissue engineering, orthopedic scaffolds, piezoresistive sensing, polyetheretherketone nanocomposites, smart lattices

Received: October 10, 2023

Revised: December 1, 2023

Published online:

- [1] M. He, Y. Huang, H. Xu, G. Feng, L. Liu, Y. Li, D. Sun, L. Zhang, *Acta Biomater.* **2021**, 129, 18.
- [2] F. Herold, A. Schneller, *Adv. Mater.* **1992**, 4, 143.
- [3] J. Denault, M. Dumouchel, *Adv. Perform. Mater.* **1998**, 5, 83.
- [4] S. M. Kurtz, J. N. Devine, *Biomaterials* **2007**, 28, 4845.
- [5] A. Haleem, M. Javaid, *Clin. Epidemiol. Global Health* **2019**, 7, 571.
- [6] S. M. Kurtz, in *Plastics Design Library* (Ed: S.M.B.T.-P.B.H. (Second E. Kurtz)), William Andrew Publishing, New York, USA **2019**, p. 3.
- [7] B. Di Maggio, P. Sessa, P. Mantelli, P. Maniscalco, F. Rivera, G. M. Calori, L. Bisogno, G. Scaravilli, M. Caforio, *Injury* **2017**, 48, S34.
- [8] M. Navarro, A. Michiardi, O. Castaño, J. A. Planell, *J. R. Soc. Interface* **2008**, 5, 1137.
- [9] J. Döring, M. Crackau, C. Nestler, F. Welzel, J. Bertrand, C. H. Lohmann, *J. Mech. Behav. Biomed. Mater.* **2019**, 97, 212.
- [10] F. Mussano, T. Genova, L. Munaron, M. G. Faga, S. Carossa, *Dental Implantology and Biomaterial*, IntechOpen, London, UK **2016**.
- [11] C. G. Ambrose, B. E. Hartline, T. O. Clanton, W. R. Lowe, W. C. McGarvey, in *Advanced Polymers in Medicine* (Ed: F. Puoci), Springer International Publishing, Cham **2015**, p. 129.
- [12] G. Szczyński, M. Kopec, D. J. Politis, Z. L. Kowalewski, A. Łazarski, T. Szolc, *Materials* **2022**, 15, 3622.
- [13] S. Najeeb, Z. Khurshid, S. Zohaib, M. S. Zafar, *J. Oral Implantol.* **2016**, 42, 512.
- [14] R. Ma, J. Wang, C. Li, K. Ma, J. Wei, P. Yang, D. Guo, K. Wang, W. Wang, *J. Biomater. Appl.* **2020**, 35, 342.
- [15] T. Wan, Z. Jiao, M. Guo, Z. Wang, Y. Wan, K. Lin, Q. Liu, P. Zhang, *Bioact. Mater.* **2020**, 5, 1004.
- [16] T. Gültan, M.Ç. Yurtsever, M. Gümüşderelioglu, *Biomed. Mater.* **2020**, 15, 035019.
- [17] J. W. Durham, S. A. Montelongo, J. L. Ong, T. Guda, M. J. Allen, A. Rabiei, *Mater. Sci. Eng. C* **2016**, 68, 723.
- [18] Z. Zheng, P. Liu, X. Zhang, J. Xin, Y. Wang, X. Zou, X. Mei, S. Zhang, S. Zhang, *Mater. Today Bio* **2022**, 16, 100402.
- [19] K. Rodzeń, P. K. Sharma, A. McIlhagger, M. Mokhtari, F. Dave, D. Tormey, R. Sherlock, B. J. Meenan, A. Boyd, *Polymers* **2021**, 13, 545.
- [20] K.-T. Kang, Y.-G. Koh, J. Son, J. S. Yeom, J.-H. Park, H.-J. Kim, *Composites, Part B* **2017**, 130, 248.
- [21] N. Baneshi, B. K. Moghadas, A. Adetunla, M. Y. P. M. Yusuf, M. Dehghani, A. Khandan, S. Saber-Samandari, D. Toghraie, *J. Mater. Res. Technol.* **2021**, 15, 5526.
- [22] C. E. Gillman, A. C. Jayasuriya, *Mater. Sci. Eng. C* **2021**, 130, 112466.
- [23] C. Liao, Y. Li, S. C. Tjong, *Polymers* **2020**, 12, 2858.
- [24] B. I. Oladapo, S. A. Zahedi, S. O. Ismail, D. B. Olawade, *Renewable Sustainable Energy Rev.* **2021**, 150, 111505.
- [25] C. Zhu, M. He, D. Sun, Y. Huang, L. Huang, M. Du, J. Wang, J. Wang, Z. Li, B. Hu, Y. Song, Y. Li, G. Feng, L. Liu, L. Zhang, *ACS Appl. Mater. Interfaces* **2021**, 13, 47327.
- [26] M. F. F. Arif, S. Kumar, K. M. K. Varadarajan, W. J. J. Cantwell, *Mater. Des.* **2018**, 146, 249.
- [27] S. Fateixa, M. Landauer, J. Schneider, S. Kumar, R. Böhm, *Macromol. Mater. Eng.* **2023**, 308, 2300060.
- [28] P. Verma, J. Ubaid, K. M. Varadarajan, B. L. Wardle, S. Kumar, *ACS Appl. Mater. Interfaces* **2022**, 14, 8361.
- [29] J. Ubaid, J. Schneider, V. S. Deshpande, B. L. Wardle, S. Kumar, *Adv. Eng. Mater.* **2022**, 24, 2200194.
- [30] M. U. Azam, A. Schiffer, S. Kumar, *Composites, Part A: Appl. Sci. Manufact.* **2023**, 173, 107701.
- [31] Y. Wang, W.-D. Müller, A. Rumjahn, A. Schwitalla, *Materials* **2020**, 13, 466.
- [32] S. Berretta, K. Evans, O. Ghita, *Mater. Des.* **2018**, 139, 141.
- [33] S. Li, T. Wang, J. Hu, Z. Li, B. Wang, L. Wang, Z. Zhou, *J. Mech. Behav. Biomed. Mater.* **2021**, 120, 104561.
- [34] D. L. Millis, in *Canine Rehabilitation and Physical Therapy*, 2nd ed. (Eds: D. Millis, D. Levine), W. B. Saunders, St. Louis **2014**, p. 92.
- [35] F. Alam, K. M. Varadarajan, J. H. Koo, B. L. Wardle, S. Kumar, *Adv. Eng. Mater.* **2020**, 22, 2000483.
- [36] A. Mora, P. Verma, S. Kumar, *Composites, Part B* **2020**, 183, 107600.
- [37] W. Zhang, A. A. Dehghani-Sani, R. S. Blackburn, *J. Mater. Sci.* **2007**, 42, 3408.
- [38] M. Mohiuddin, S. V. Hoa, *Compos. Sci. Technol.* **2011**, 72, 21.
- [39] J. Gonçalves, P. Lima, B. Krause, P. Pötschke, U. Lafont, J. R. Gomes, C. S. Abreu, M. C. Paiva, J. A. Covas, *Polymers* **2018**, 10, 925.
- [40] M. He, C. Zhu, H. Xu, D. Sun, C. Chen, G. Feng, L. Liu, Y. Li, L. Zhang, *ACS Appl. Mater. Interfaces* **2020**, 12, 56924.
- [41] N. Jiang, P. Tan, M. He, J. Zhang, D. Sun, S. Zhu, *Polym. Test.* **2021**, 100, 107276.
- [42] J. Schneider, S. Kumar, *J. Mater. Res. Technol.* **2023**, 26, 7182.
- [43] Apium P220 - Industrial 3D printer for high performance materials, Apium, <https://apiumtec.com/en/industrial-3d-printer> (accessed: August 2023).
- [44] Q. M. Li, I. Magkiriadis, J. J. Harrigan, *J. Cell. Plast.* **2006**, 42, 371.
- [45] Standard Test Method for Compressive Properties of Rigid Cellular Plastics, <https://www.astm.org/d1621-16.html> (accessed: May 2023).
- [46] S. H. Kim, G. W. Mulholland, M. R. Zachariah, *Carbon* **2009**, 47, 1297.
- [47] Victrex High Performance PAEK Polymers, Victrex PEEK 450G **2019**, [https://www.victrex.com/-/media/downloads/datasheets/victrex\\_tds\\_450g.pdf](https://www.victrex.com/-/media/downloads/datasheets/victrex_tds_450g.pdf) (accessed: June 2021).
- [48] P. Pötschke, M. Abdel-Goad, I. Alig, S. Dudkin, D. Lellinger, *Polymer* **2004**, 45, 8863.
- [49] R. Socher, B. Krause, M. T. Müller, R. Boldt, P. Pötschke, *Polymer* **2012**, 53, 495.
- [50] P. B. Tamba, A. R. Bhattacharyya, A. R. Kulkarni, *J. Appl. Polym. Sci.* **2013**, 127, 1017.
- [51] R. Shrestha, J. Simsirivong, N. Shamsaei, R. D. Moser, *Int. J. Fatigue* **2016**, 82, 411.
- [52] P. Verma, J. Ubaid, F. Alam, S. Deveci, S. Kumar, *Def. Technol.* **2023**, 30, 13.